Supplementary Information for:

Ultrahigh-temperature film capacitors via homo/heterogeneous interfaces

Rui Lu[1,2†], Zhonghui Shen[3,4†], Chunrui Ma[2†*], Tingzhi Duan[1,2], Lu Lu[1,2], Guangliang Hu[1,2], Tian-Yi Hu[2], Caiyin You[5], Shaobo Mi[2*], Chun-Lin Jia[1,2,6], Long-Qing Chen[7*], Ming Liu[1,2*]

†These authors contributed equally to this work.

*Corresponding author. Email: chunrui.ma@xjtu.edu.cn (C. Ma), shaobo.mi@xjtu.edu.cn (S.-B. Mi), lqc3@psu.edu (L.-Q. Chen), m.liu@xjtu.edu.cn (M. Liu).

This PDF file includes:

Methods

Phase-field Simulations

In this work, we design four representative dielectrics to study the interface effect on energy storage: pure matrix (PM), vertical interface (VI), parallel interface (PI) and interlayer interface (II), as shown in Figure 1(a)-1(d). In the phase-field model, we introduce an order parameter $\eta(\mathbf{r},t)$ to describe the dielectric response under different electric fields, including polarization and breakdown process. $\eta(\mathbf{r},t)$=1 represents the breakdown phase, $\eta(\mathbf{r},t)$=0 represents the non-breakdown phase. Here, the free energy in inhomogeneous system includes the phase separation f_{sep}, the gradient energy f_{grad} and electrostatic energy density f_{elec} as follows:

$$F=\int_V\left[f_{\text{sep}}\left(\eta(\mathbf{r})\right)+f_{\text{grad}}\left(\eta(\mathbf{r})\right)+f_{\text{elec}}\left(\eta(\mathbf{r})\right)\right]dV \tag{S1}$$

Here, the phase separation energy is defined by a double-well function,

$$f_{\text{sep}}\left(\eta(\mathbf{r})\right)=\alpha\eta^2(1-\eta)^2 \tag{S2}$$

where α is a positive coefficient describing the energy barrier of the phase separation with a value of 10^8 J/m^3 in this work. The gradient energy is expressed as

$$f_{\text{grad}}\left(\eta(\mathbf{r})\right)=\frac{1}{2}\gamma\left|\nabla\eta(\mathbf{r})\right|^2 \tag{S3}$$

where γ is the gradient energy coefficient with the value of 10^{-10} J/m. The electrostatic energy can be calculated by

$$f_{\text{elec}}\left(\eta(\mathbf{r})\right)=-\frac{1}{2}\varepsilon_0\varepsilon_{ij}(\mathbf{r})E_i(\mathbf{r})E_j(\mathbf{r}) \tag{S4}$$

where $\varepsilon_{ij}(\mathbf{r})$ is the spatially dependent permittivity, $E_i(\mathbf{r})$ is the total electric field component. In order to describe the matrix and the nanofillers in the nanocomposite, a non-evolving field variable $\rho(\mathbf{r})$ is introduced, which takes the value of 1 in the

interface phase and 0 in the matrix. Then, the spatially dependent permittivity could be written as:

$$\begin{aligned}\varepsilon_{ij}(\mathbf{r}) = \eta^3\left(10-15\eta+6\eta^2\right)\varepsilon_{ij}^{\mathrm{B}} + \left[1-\eta^3\left(10-15\eta+6\eta^2\right)\right]\times \\ \left\{\rho^3\left(10-15\rho+6\rho^2\right)\varepsilon_{ij}^{\mathrm{I}} + \left[1-\rho^3\left(10-15\rho+6\rho^2\right)\right]\varepsilon_{ij}^{\mathrm{M}}\right\}\end{aligned} \tag{S5}$$

where $\varepsilon_{ij}^{\mathrm{B}}$, $\varepsilon_{ij}^{\mathrm{I}}$, and $\varepsilon_{ij}^{\mathrm{M}}$ indicate the permittivity of the breakdown phase, interface phase, and the matrix, respectively.

A modified Allen-Cahn equation is developed to govern the dynamic process of dielectric breakdown,

$$\frac{\partial\eta(\mathbf{r},t)}{\partial t} = -L_0 H\left(|f_{\mathrm{elec}}|-|f_{\mathrm{critical}}|\right)\left[\frac{\partial f_{\mathrm{sep}}(\eta)}{\partial\eta(\mathbf{r},t)} - \gamma\nabla^2\eta(\mathbf{r},t) + \frac{\partial f_{\mathrm{elec}}(\mathbf{r})}{\partial\eta(\mathbf{r},t)}\right] \tag{S6}$$

where L_0 is the kinetic coefficient determining the interface mobility, $H(|f_{\mathrm{elec}}|-|f_{\mathrm{critical}}|)$ is the Heaviside unit step function ($H(|f_{\mathrm{elec}}|<|f_{\mathrm{critical}}|)=0$ and $H(|f_{\mathrm{elec}}|>|f_{\mathrm{critical}}|)=1$), and f_{critical} is the maximal energy density calculated by $f_{\mathrm{critical}} = \frac{1}{2}\varepsilon_0\varepsilon_{\mathrm{r}}E_{\mathrm{b}}^2$. The local electric field distribution could be calculated by solving Poisson's equation using the spectral iterative perturbation method as follows:

$$\nabla D = \nabla\left(\varepsilon_0\varepsilon_r E(\mathbf{r})\right) = 0 \tag{S7}$$

Here, the characteristic length scale $d_0 = \sqrt{\gamma/\alpha}$, and the characteristic time scale $t_0=1/(L_0\alpha)$ can be defined in terms of the material parameters γ, α and L_0. A grid size of $N_x\Delta x\times N_y\Delta x\times N_z\Delta x$ with grid space of $\Delta x=d_0$ is employed with $N_x=N_y=512$ and $N_z=1$. The field-dependent permittivity is calculated from the ferroelectric hysteresis loop in experiments.

Then, the heat transport process is described by

$$\rho(\mathbf{r})c_p(\mathbf{r})\frac{\partial T(\mathbf{r},t)}{\partial t}=\kappa(\mathbf{r})\nabla T^2(\mathbf{r},t)+\sigma(\mathbf{r},T)E^2 \quad \text{(S8)}$$

where ρ, c_p, κ and σ are the density, constant-pressure heat capacity, thermal conductivity and electrical conductivity, respectively. The applied electric field is fixed at 14 MV/m, and the heat flux at boundaries is assumed to be controlled by the convective heat transfer by

$$n(-\kappa\nabla T)=h(T-T_{\text{sur}}) \quad \text{(S9)}$$

where T_{sur} is the surrounding temperature with a value of 293K and h is the convective heat transfer coefficient with a value of 10 W/m^{-2} K^{-1}. To reflect the differences of matrix and interface phase on electrical and thermal properties, the electrical conductivities are set with $1e^{-8}$ S m^{-1} for matrix and $1e^{-10}$ S m^{-1} for interface phase, and the thermal conductivities are considered as 12 W m^{-1} K^{-1} for interface phase and 7 W m^{-1} K^{-1} for matrix.

Target and film fabrication

A series of stoichiometric $BaHf_xTi_{1-x}O_3$(BHTO) ceramic targets (x = 0.17,0.25 and 0.32) were prepared by the conventional solid-state sintering methods[28]. High-purity $BaCO_3$, TiO_2 and HfO_2 (purity 99.99%) powders were mixed at designed stoichiometric ratios, ball-milled for 4 hours and then calcined at 850 ℃ for 4 hours. The calcined powder was further ball milled to reduce the particle size. Alcohol solution was added to the dried powder as a binder, and the powder was pressed into pellets with diameters of 50 mm at 15 MPa for 15 min. After the binder was burned out at 650 ℃ for 2 h, the pellets were sintered at 1050 ℃ for 2 h in a sealed alumina crucible.

Both targets ware pre-sputtered for 12 h to eliminate any potential contaminant on the surface.The BHTO films were fabricated on 0.7% Nb doped (001)-oriented Nb:STO

single-crystalline substrates using the adio frequency magnetron sputtering system with different growth temperature of 700 ℃ and 850 ℃. The combined effects of the strain engineering and the different energy barrier for diffusion supplied by different growth temperature enabled us to modify the grains size and grain orientation in the films. The optimal growth conditions were found of 0.135 mbar with the mixed ambient of Ar and O_2 in the ratio of 1 : 1. After that, the films were annealed in an oxygen-enriched environment (~200 mbar) for 15 min, and then cooled down at a rate of 10 ℃ min^{-1} to room temperature. The multilayers were achieved through alternately growing the BHTO layers with different Hf^{4+}content and the layer thickness was controlled by the deposition time for each layer. All the film thicknesses were controlled to be ~400 nm by controlling the deposition time and further confirmed by scanning electron microscopy (SEM, FEI Quanta FEG 250).

Characterizations

The phase and epitaxial properties of the films were characterized by high resolution X-ray diffractometer (HRXRD; PANalytical X'Pert MRD) with Cu Kα radiation (λ = 1.540598 Å). HAADF-STEM images and EDS mapping were investigated on a scanning transmission electron microscopy (JEOL ARM 200F), equipped with a probe aberration corrector, operated at 200 keV. Before the dielectric and ferroelectric measurements, Pt top electrodes (a set of square electrode with the size of 200 μm × 200 μm and ~45 nm in thickness) were sputtered through a stainless-steel shadow mask by using sputtering system. The electric field was applied as the top-

to-bottom electrode configuration. Measurements of the dielectric permittivity and loss tangent over broad frequency and temperature ranges were conducted on a precision impedance analyzer (HP-4980A, Agilent) with a perturbation voltage of 1 V. The DC bias voltage of the dielectric measurements were set as 0 V. The hysteresis loops of polarization versus electric field (*P*-*E*) in the were recorded by a ferroelectric tester (TF2000 analyzer; axi ACCT, Aachen, Germany). Unipolar hysteresis *P*-*E* loops, from which the energy storage density and efficiency were derived, were collected using unipolar triangular voltage waves with a frequency of 1 kHz. The first order reversal curve (FORC) loops were measured using biased half- triangular electric field pulses of E_{max}=3.75 MV/cm and $\Delta E_r = \Delta E$= 0.125 MV/cm and 60 FORC loops were measured with 40 Hz. For the fatigue behavior for charging-discharging cycling test, successive bipolar triangular voltage waves were applied on the films; after that, a unipolar field was applied to characterize the *P*-*E* loops and energy storage performance. The leakage currents were characteristics with a delay time of 2 s were measured using an Agilent B2901A precision source. A different temperature environment was provided through a Lakeshore cryocooled probe station (CRX-6.5K, Lake Shore Cryotronics, Inc., USA). The fast discharge experiments were carried out in a capacitor charge−discharge test system (PK-CPR 1701-15012, PolyK Technologies, PA, USA).

Weibull distribution

The values of breakdown electric field (E_b) are analyzed with a two-parameter Weibull distribution function[26], as shown in equation (S10):

$$P_i = 1 - \exp[-(E_i / E_b)^{\beta}] \tag{S10}$$

The equation above can also be described by :

$$\ln(1 - P_i) = \ln[\exp -(E_i / E_b)^{\beta}] = -(E_i / E_b)^{\beta} \tag{S11}$$

$$\ln\{\ln[1/(1 - P_i)]\} = \beta[\ln(E_i) - \ln(E_b)] \tag{S12}$$

Here, we define:

$$X_i = \ln(E_i) \tag{S13}$$

$$Y_i = \ln\{\ln[1/(1 - Pi)]\} \tag{S14}$$

$$P_i = i/(n+1) \tag{S15}$$

So the calculation formula is:

$$Y_i = \beta[X_i - \ln(E_b)] \tag{S16}$$

Where E_i is the experimental breakdown strength of the ith dataset arranged in ascending order ($E_1 \le E_2 \le E_3 \ldots\ldots \le E_n$), β is the shape parameter associated with linear regressive fit of the data distribution, P_i is the cumulative probability of dielectric breakdown, and n is the total number of dates for each film. According to the equation above, the X_i and Y_i have a linear relationship.

Supplementary Text

Analying the leakage mechanisms in the BHTO films

Five leakage mechanisms fall into two categories,bulk-limited and interface-limited[36]. Ohmic conduction, space charge limited conduction (SCLC) and Poole-Frenkel (P-F) emission are the bulk-limited mechanisms. The bulk-limited conduction mechanism dends on the electrical properties of the dielectric itself[3]. Schottky emission and Fowler-Nordheim (F-N) tunnelling are interface-limited ones, which the electrons overcome the energy barrier at the metal-dielectric interface to go to the dielectric. The mathematical formulas of the mechanisms based on leakage density (J) and electric field (E) can be expressed as:

Ohmic: $$J = en\mu E\ , \tag{S17}$$

SCLC: $$J = \frac{9\mu\varepsilon_0\varepsilon_r}{8}\cdot\frac{E^2}{d}\ , \tag{S18}$$

P-F emission: $$J = e\mu N_c E\cdot\exp\left[-\frac{\Phi_{\mathrm{PF}}}{k_B T}+\frac{1}{k_B T}\left(\frac{e^3 E}{\pi\varepsilon_0 K}\right)^{1/2}\right], \tag{S19}$$

Schottky emission: $$J = AT^2\cdot\exp\left[-\frac{\Phi_{\mathrm{Schottky}}}{k_B T}+\frac{1}{k_B T}\left(\frac{e^3 E}{4\pi\varepsilon_0 K}\right)^{1/2}\right], \tag{S20}$$

F-N tunnelling: $$J = \frac{e^2E^2}{8\pi h\phi_B}\cdot\exp\left[\frac{-8\pi\left(2em_T^*\right)^{1/2}}{3hE}\phi_B^{3/2}\right], \tag{S21}$$

Where $e, n, \mu, \varepsilon_0, \varepsilon_r, d, N_c, \Phi_{\mathrm{PF}}, k_B, T, K, A, \Phi_{\mathrm{schottky}}, h, m_T^*$ are electronic charge, electron density,electronic drift mobility, vaccum permittivity, relative permittivity, film thickness,effective density of states of the conduction band, P-F emission energy barrier, Boltzmann constant, absolute temperature, optical permittivity ,Richardson constant, Schottky energy barrier, Plank constant, potential barrier height,effective electron mass

and, respectively. The K equals the square of the optical refractive index n. The n of HfO_2 and $BaTiO_3$ are around 1.98 and 2.49, respectively[3,37], the K value of the BHTO films should be 3 ~ 7. Figure S5 shows the fitting results based on each mechanism. Figure. S3A shows ln (J) vs ln (E) for the films at a positive bias,which shows three characteristic linear regions. In region (i), at a lower bias (E < E1), the plots are linear with a slope around 1, indicating that an Ohmic conduction behavior plays the dominant role in the electric field range. at $E > E_{TEL}$(called the trap-filled limit electric field), the slope is much greater than 2, indicating that the trap is filled and the leakage current sharply increases to a situation equivalent to no trap. Through increasing the interface of the films, we can significantly increase the E_1 and E_{TEL} and accordingly improve the leakage and breakdown properties of the BHTO thin films. At high electric fields, the fitting results exclude P-F tunnelling mechanism, since the ε_{PF} values calculated from slopes of ln (J/E) vs $E^{1/2}$ plots are one order of magnitude larger than 7. Fittings with F-N and Schottky emissions (Supplementary Fig. 5 C and D) both show linear patterns at high electric fields, and FN tunneling has been identified as the dominant leakage mechanism at a high electric field for all of the BHTO films, However,only HOI@HEI@II sample is suggesting a Schottky emission at high electric field.

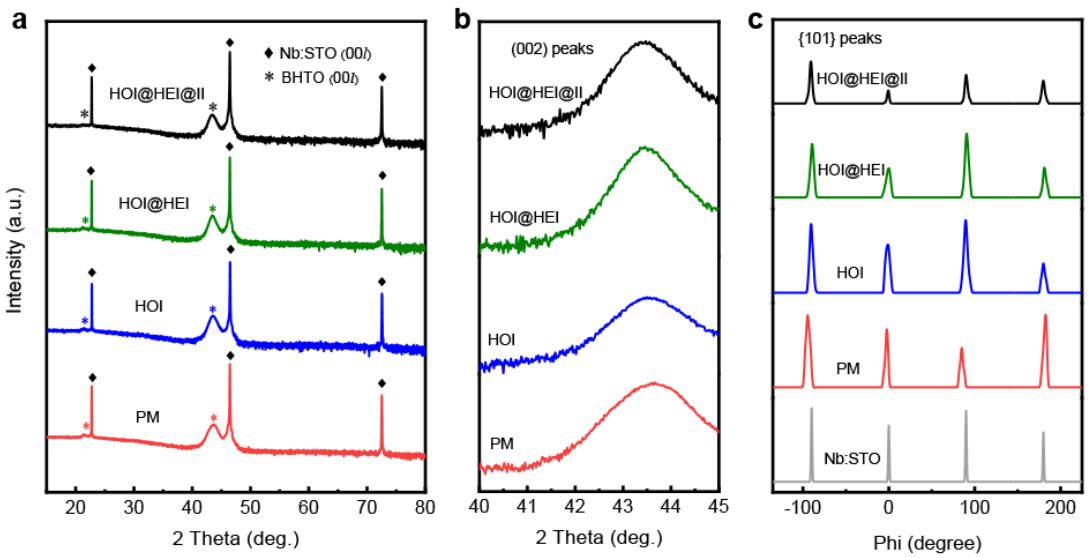

Supplementary Fig. 1|XRD patterns of the BHTO films. (a) Theta-2theta, (b) Enlarged *θ-2θ* scans near the (002) peak. and (c) phi scans of the BHTO films. All the films are pure perovskites with highly (00*l*) orientations inherited from the substrates. Phi scans further demonstrate the fourth-fold symmetry of the films with a cubic-on-cubic single-crystalline epitaxy.

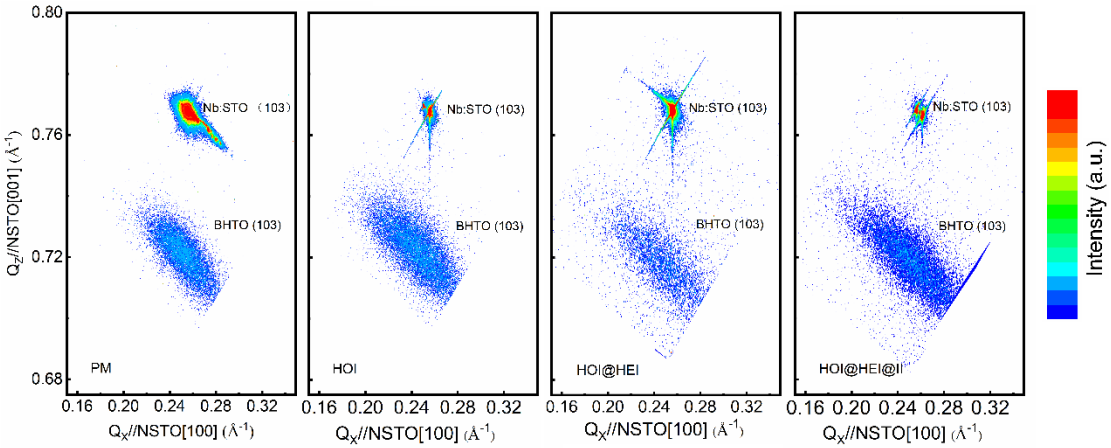

Supplementary Fig. 2|Reciprocal space maps results for PM, HOI, HOI@HEI and HOI@HEI@II films around the Nb:STO (103) diffraction spots. Increasing the interface, the spots on the films are gradually stretched.

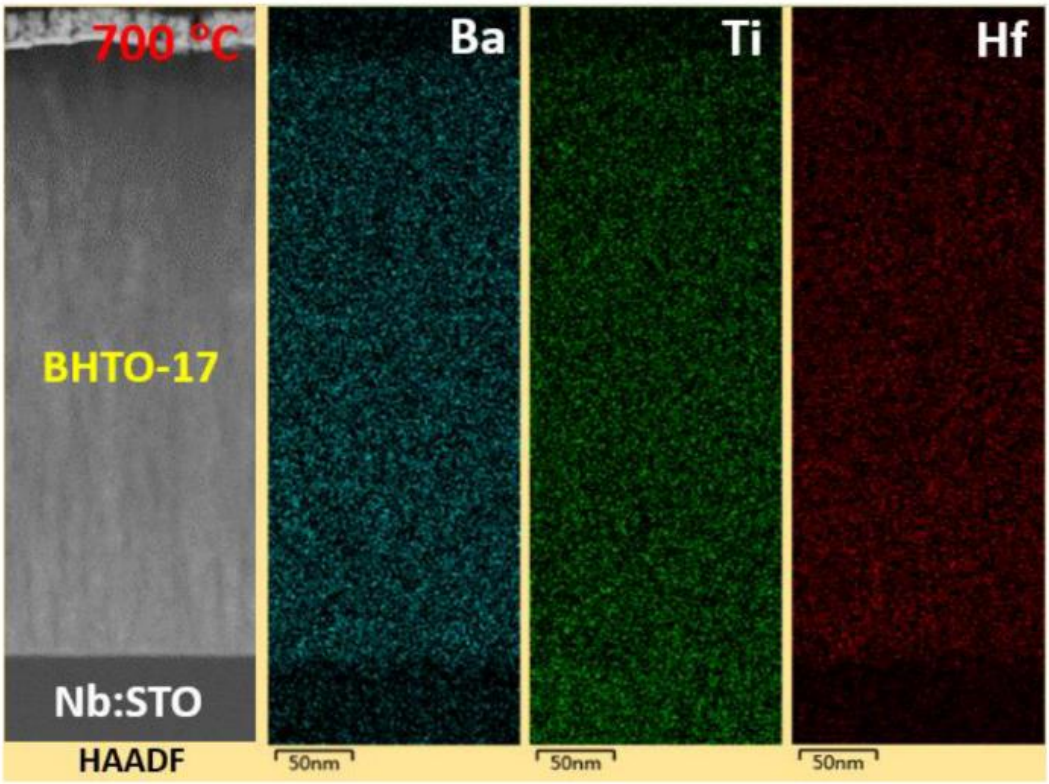

Supplementary Fig. 3|No apparent elemental segregation in the BHTO-17 films by energy-dispersive X-ray spectroscopy (EDS) mapping. A HAADF-STEM image of BHTO-17 films prepared on Nb-doped $SrTiO_3$ (001) (Nb:STO) substrates at 700°C, and the corresponding elemental maps of Ba, Ti and Hf, which indicates no apparent elemental segregation in the BHTO-17 films. The HAADF-STEM image is viewed along the [010] direction of the Nb:STO substrate.

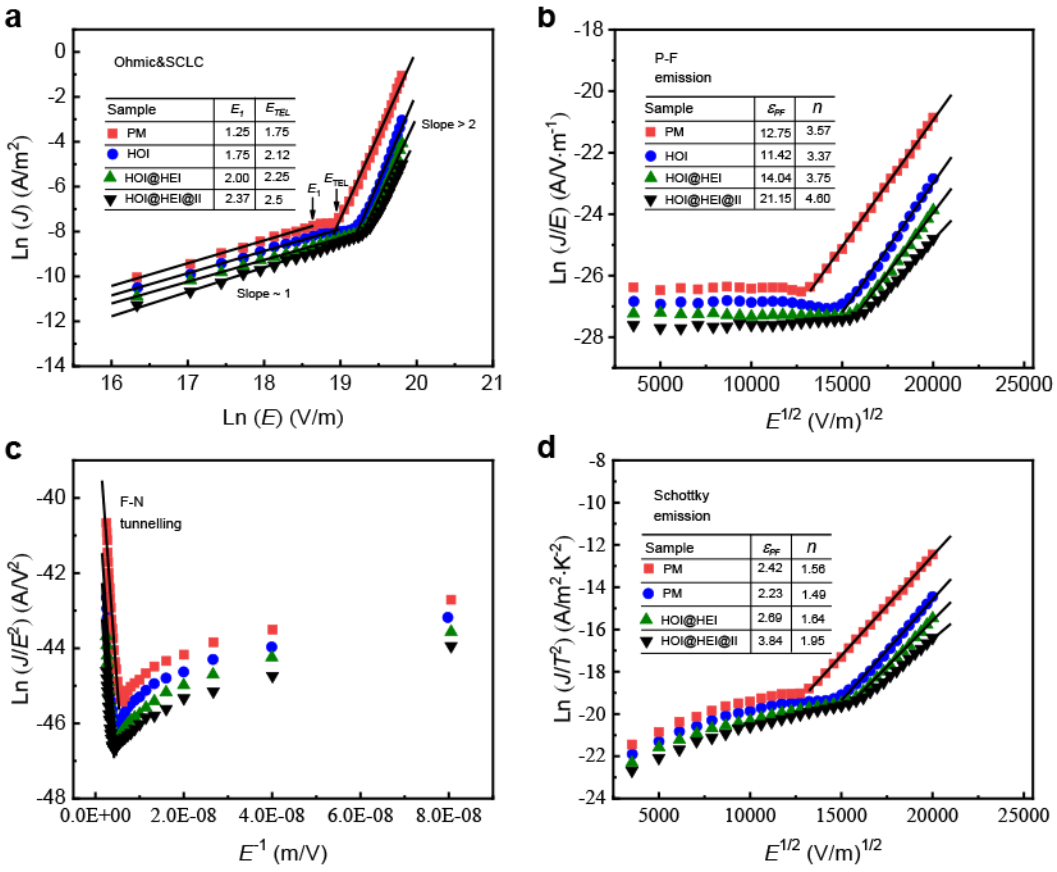

Supplementary Fig. 4|Fittings of the leakage current densities of the BHTO films with various conduction mechanisms. (a) Ohmic conduction and space charge limited conduction (SCLC), (b) P-F emission, (c) F-N tunnelling and (d) Schottky emission.

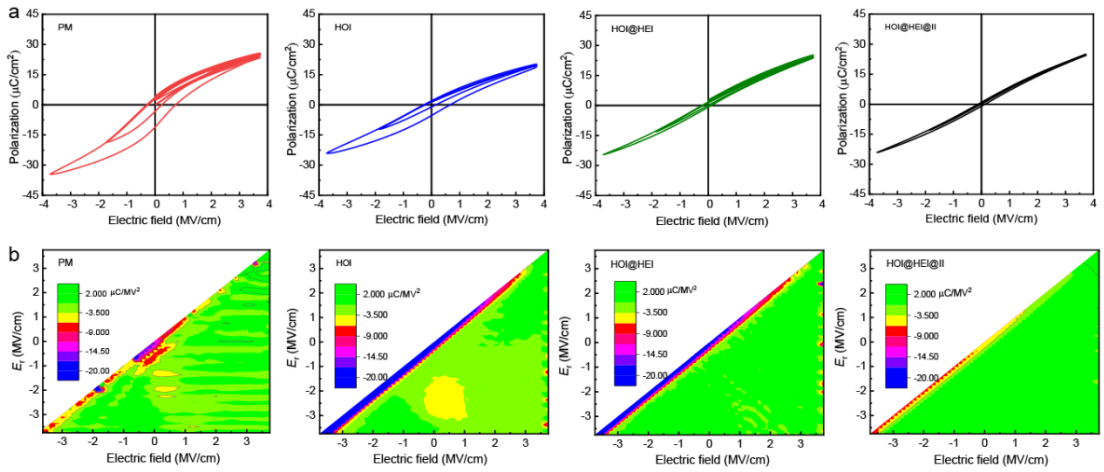

Supplementary Fig. 5|FORC loops and corresponding evolution distribution of the BHTO films. (a) FORC loops of the BHTO films, (only four out of the total 60 loops are shown for clarity). (b) Corresponding FORC distribution $\rho(E_r,E)$ of the BHTO thin films. The diagram of the PM film exhibits a low-intensity distribution zone located near the origin point, which reflects the typical ferroelectric state and strongly nonlinear polarization .With increasing the interface, the $\rho(E_r,E)$ becomes more evenly distributed in the whole electric field range, indicating further weakened FE nonlinearity and dispersed polarization contribution in the RFE state.

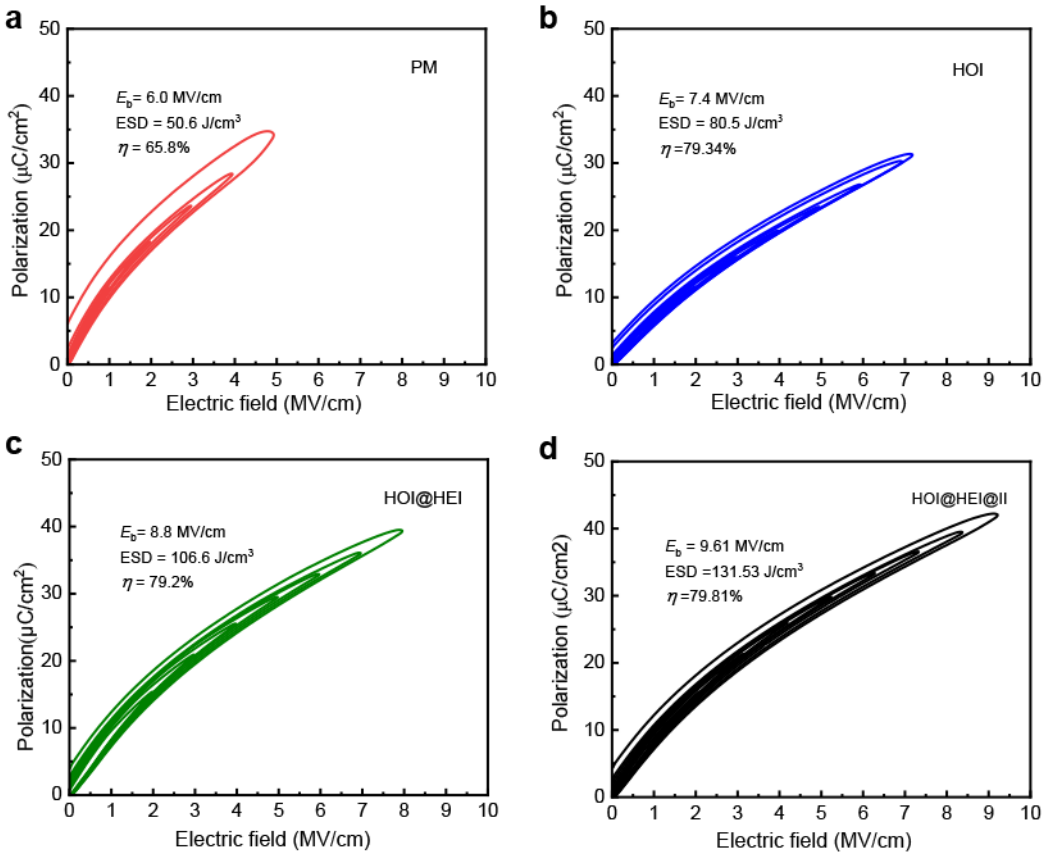

Supplementary Fig. 6|Unipolar *P-E* loops of the BHTO films at 1 kHz. (a) PM, (b) HOI, (c)HOI@HEI, and (d) HOI@HEI@II.

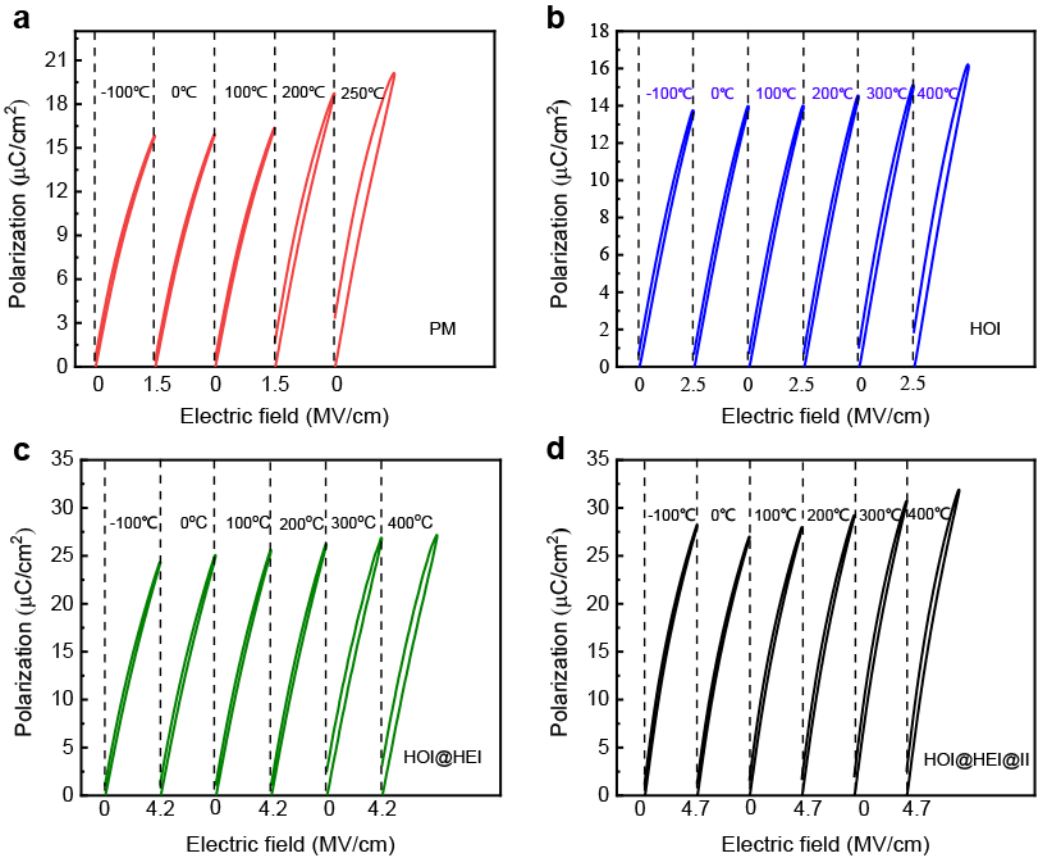

Supplementary Fig. 7|Unipolar *P-E* loops of the BHTO films measured at various temperatures under differrent electric field. (a) PM at 1.5 MV/cm, (b) HOI at 2.5MV/cm, (c) HOI@HEI at 4.2MV/cm and (d) HOI@HEI@II at 4.7MV/cm.

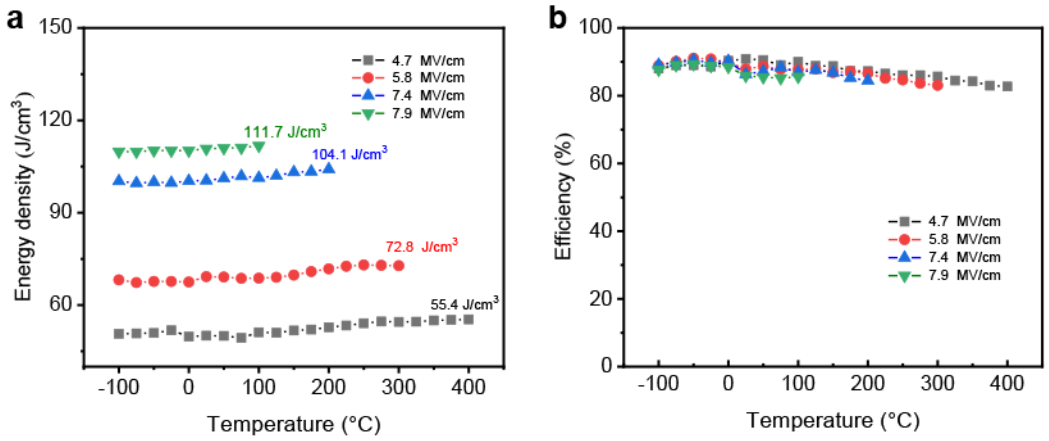

Supplementary Fig. 8|Temperature-dependent (a) energy density and (b) efficiency of the HOI@HEI@II film at different electric fields.

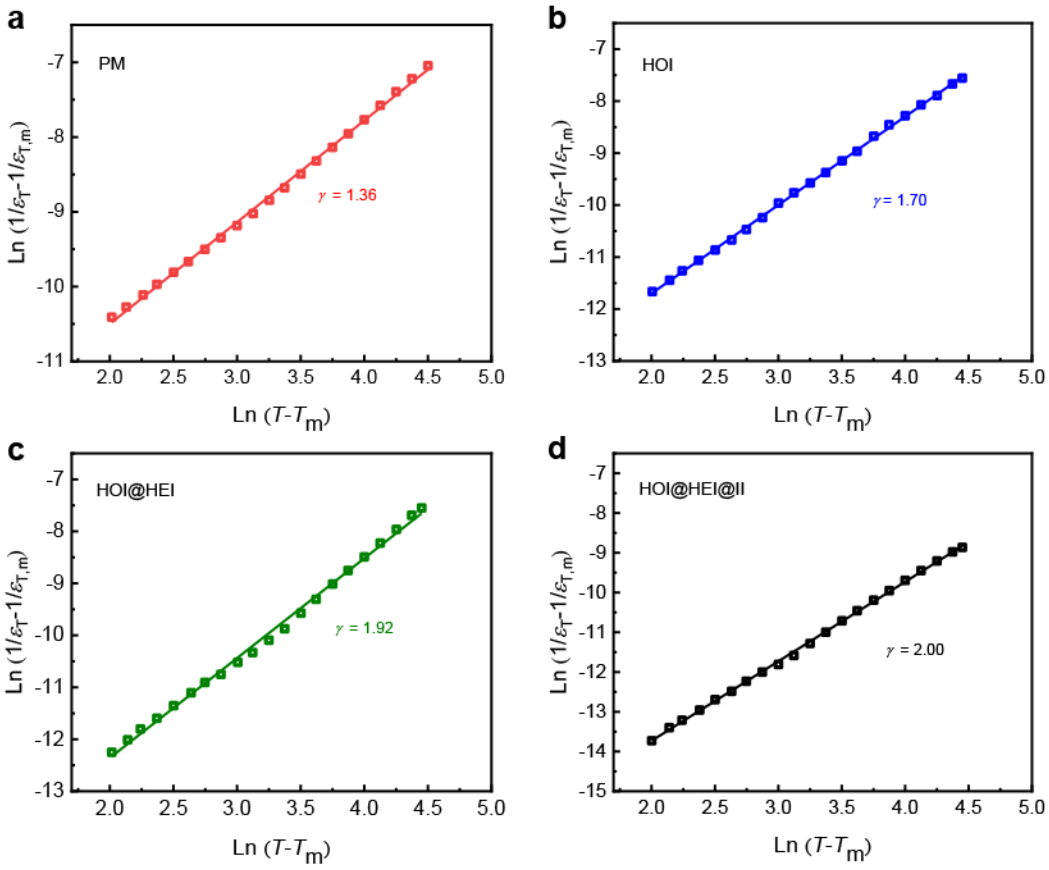

Supplementary Fig. 9|Fittings of the relaxor factor γ of BHTO films with the modified Curie-Weiss law. Plots of $\ln(1/\varepsilon_T - 1/\varepsilon_{T,m})$ versus $\ln(T - T_m)$ of BHTO films at the frequency of 1 MHz.The relaxor feature of the RFE films can be quantitatively described by the diffuseness factor (γ), which value between 1 (normal ferroelectrics) to 2 (ideal relaxor ferroelectrics). The value of γ increases gradually from 1.36 to 2.00 with increasing the interface. The factor γ can be derived from the modified Curie-Weiss law

$$\frac{1}{\varepsilon_r} - \frac{1}{\varepsilon_{r,m}} = \frac{(T - T_m)^{\gamma}}{C} \tag{S12}$$

Where ε_r is the permittivity at the temperature T; T_m is the temperature at which ε_r reaches the maximum $\varepsilon_{r,m}$. C is a constant.

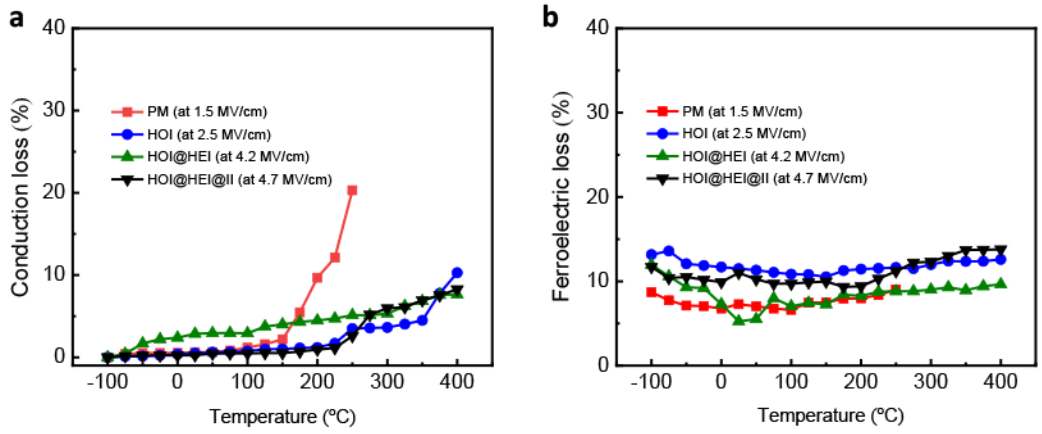

Supplementary Fig. 10|Temperature-dependent conduction and ferroelectric loss. (a) Conduction loss and (b) ferroelectric loss of the BHTO films measured at varied fields. To investigate the effect of different contribution sources of hysteresis loss, the conduction loss is derived from the *P*–*E* loops with the reasonable assumption that the remnant polarization P_r at -100 ℃ is all originated from ferroelectric loss and the increased part at higher temperatures (i.e., $P_{cond} = P_r$ (T) - P_r (T = -100 ℃)) all comes from the conduction loss[16]; therefore the effective conductivity σ_{eff} and the conduction loss U_{cond} can be calculated by the following equations:

$$P_{cond} = \frac{1}{2} \cdot \sigma_{eff} E^2 T \tag{S13}$$

$$U_{cond} = \frac{1}{3} \cdot \sigma_{eff} E^2 T \tag{S14}$$

where T is the period of the applied electric field. After σ_{eff} is determined, The ferroelectric loss can be subtracted from the total dielectric loss to give the conduction loss. Supplementary Fig. 10(a)and(b) present the conduction loss and ferroelectric loss of he BHTO films at different electric fields, respectively.The results show that the homogeneous and heterogeneous interfaces efficiently suppress the conduction loss at higher temperatures, leading to the thermal stabilization and high operating temperature

of energy performance for engineered film.

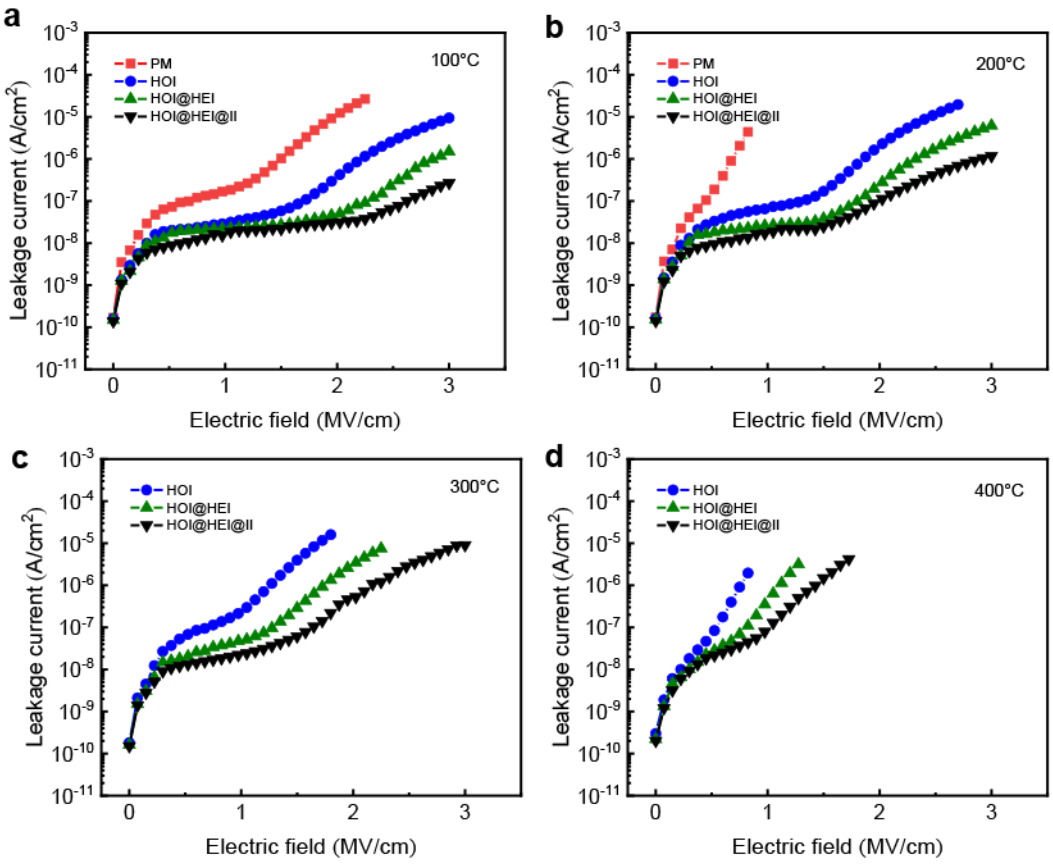

Supplementary Fig. 11|Leakage current densities of the BHTO films as a function of the biased electric field at various temperatures. (a) at 100 ℃, (b) at 200 ℃,(c) at 300 ℃ and (d) at 400 ℃.

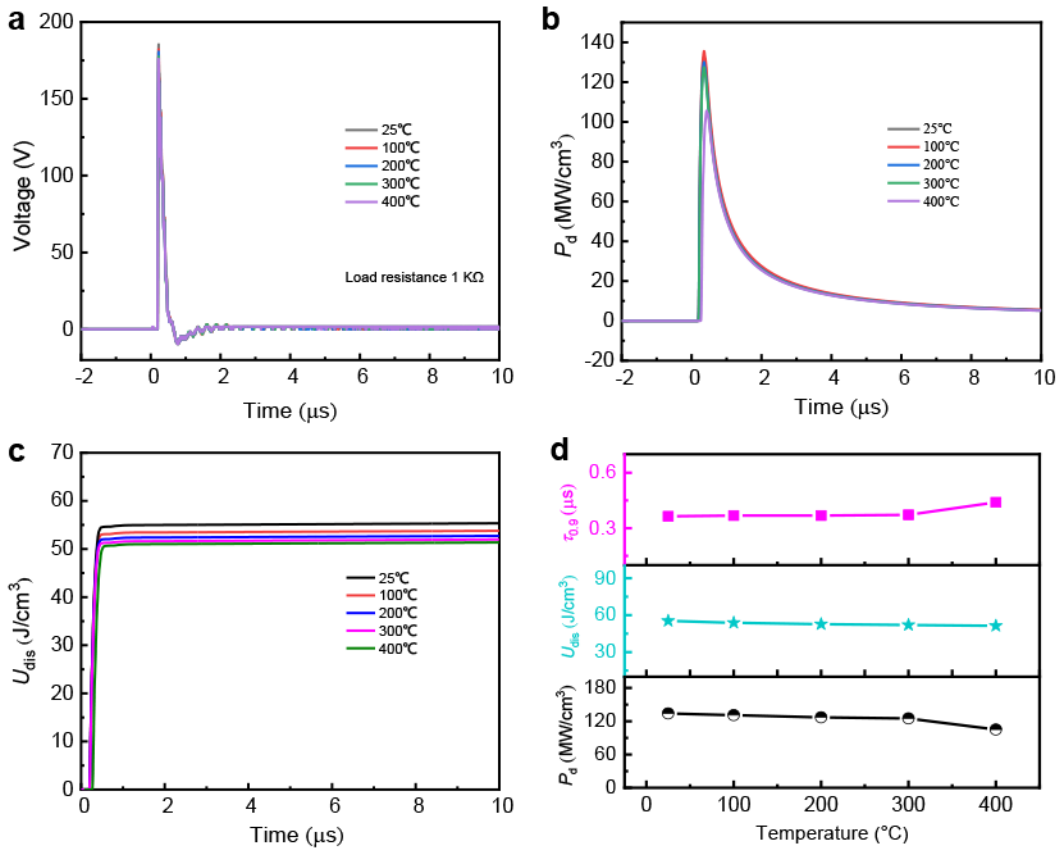

Supplementary Fig. 12|The energy discharge behaviors and power density performance of the HOI@HEI@II BHTO film at various temperatures. (a) Discharge voltage curve at different temperatures, (b) power density (P_d) of at 4 MV/cm. (c) The discharged energy density (U_{dis}) at different temperatures. (d) The temperature stability of P_d, U_{dis}, and $\tau_{0.9}$ at different temperatures.

References

36. Fan, Q. L. et al. Manipulating leakage behavior via thickness in epitaxial $BaZr_{0.35}Ti_{0.65}O_3$ thin film capacitors. *Appl. Phys. Lett*. **116**, 192902 (2020).

37. Han, L. et al. Broadband optical reflection modulator in indium-tin-oxide-filled hybrid plasmonic waveguide with high modulation depth. *Plasmonics*. **13**, 1309-1314 (2017).